Multi-Dimensional Reduction Clustering of Complex Carbohydrates Reveal Tissue Metabolism, Heterogeneity and Histopathology

Lindsey R. Conroy[1,2,#], Derek B. Allison[2,4,#], Qi Sun[1,#], Lyndsay E.A. Young[3], Tara R. Hawkinson[1], Harrison A. Clarke[1], Juanita E. Ferreira[4], Autumn V. Hammonds[4], Robert J. McDonald[4], Kimberly J. Absher[4], Warren J. Alilain[1,5], Christopher M. Waters[6], Jinze Liu[7] *, and Ramon C. Sun[1,2,5,8] *

[1]Department of Neuroscience, University of Kentucky College of Medicine, Lexington, KY 40536-0298, USA
[2]Markey Cancer Center, Lexington, KY 40536-0298, USA
[3]Department of Molecular and Cellular Biochemistry, University of Kentucky College of Medicine, Lexington, KY 40536-0298, USA
[4]Department of Pathology and Laboratory Medicine, University of Kentucky College of Medicine, Lexington, KY 40536, USA
[5]Spinal Cord and Brain Injury Research Center
[6]Department of Physiology, University of Kentucky College of Medicine, Lexington, KY 40536, USA
[7]Department of Biostatistics, Massey Cancer Center, Virginia commonwealth university, Richmond, VA 23284, USA
[8]Lead Contact
#Equal contribution
*Correspondence: Jinze.Liu@vcuhealth.org; ramon.sun@uky.edu

Abstract:

Formalin-fixed paraffin-embedded (FFPE) human tissues represent the world's largest collection of accessible clinical specimens with matched, well-annotated clinical course for disease progression. Currently, FFPE sections are limited to low throughput histo- and immunological assessments. Extracting largescale molecular information remains a major technological barrier to uncover the vast potential within FFPE specimens for translation and clinical research. Two critical but understudied facets of glucose metabolism are anabolic pathways for glycogen and N-linked glycan biosynthesis. Together, these complex carbohydrates represent bioenergetics, protein-structure function, and tissue architecture in human biology. Herein, we report the high-dimensional Metabolomics-Assisted Digital pathology Imaging (Madi) workflow that combines matrix-assisted laser desorption ionization mass spectrometry imaging (MALDI-MSI) with machine learning for the comprehensive assessment of tissue heterogeneity, histopathology, and metabolism in human FFPE sections. In normal human tissue sections, Madi accurately identifies anatomical regions within liver and the brain. In human lung diseases, Madi accurately predicts major lung pathologies such as honeycomb change, late-stage fibrosis, diffuse alveolar damage (DAD), and acute fibrinous and organizing pneumonia (AFOP) from idiopathic pulmonary fibrosis (IPF) and COVID-19 pneumonia specimens with precision. In depth pathway enrichment analyses reveal unique metabolic pathways are

associated with distinct pathological regions, which highlight aberrant complex carbohydrate metabolism as a previously unknown molecular event associated with disease progression that could hold key to future therapeutic interventions.

GRAPHICAL ABSTRACT

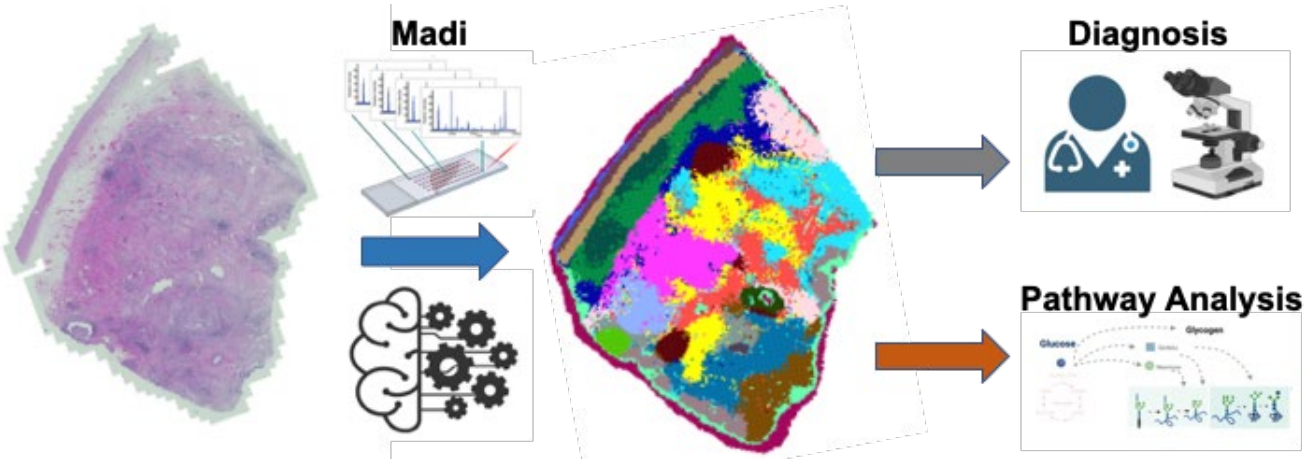

INTRODUCTION:

Mapping genotype to phenotype with near single-cell resolution and spatial definition is one of the major goals in the continuing innovations of next generation life science techniques. Recent advances in RNA sequencing technologies that allow the detailed analysis of a single isolated cell from a host tissue is a major advancement in achieving this goal. Single-cell RNA sequencing (scRNAseq) technology has incredible resolution that allows interrogation of tissue complexity and interactive networks on a cellular level (Patel et al., 2014). Thus far, scRNAseq workflow has allowed researchers to study complex cellular heterogeneity from diseased and healthy tissues, revealing complex and rare cell populations, uncovering regulatory relationships, and tracking distinct cell lineages during development (Islam et al., 2014). The next phase of technological development will include single-cell approaches capable of defining molecular features such as proteins, lipids, metabolites, and complex carbohydrates that can be mapped back to tissue architecture, bridging the gap between true genotype to phenotype analysis (Saliba et al., 2014). To this end, single-cell technologies are beginning to emerge that include cell separation-based or in situ-based lipidomic, proteomics, and glycomics (Zenobi, 2013).

Complex carbohydrates such as N-linked glycans and glycogen are terminal macro-metabolites from complex biochemical pathways (Sun et al., 2021). Anabolic pathways for the biosynthesis of glycogen and N-linked glycans span multiple cellular compartments including the nucleus, cytoplasm, endoplasmic reticulum, Golgi, and finally the plasma membrane (Stanley et al., 2017). Together, complex carbohydrates modulate a myriad of cellular functions including bioenergetics, epigenetics, protein-ligand binding, membrane transport activity, and protein turnover (Yan and Lennarz, 2005). N-linked glycans especially, are critical structural components of tissue architecture, vital for immune modulation and organ function (Rudd et al., 1999). They are highly concentrated at cellular junctions such as tight junctions, gap junctions, stroma, and extracellular matrix and play critical roles in cell-to-cell adhesion and communication (Gu et al., 2012; Liwosz et al., 2006). Oligomerization of simple sugars to complex carbohydrates results in increased polarity and decreased solubility, therefore qualitive and spatial analyses of complex carbohydrates remain challenging. A new technique was developed recently, employing enzyme-assisted MALDI-MSI that can simultaneously perform spatial profiling of both glycogen and N-linked glycans from FFPE mammalian sections *in situ*, preserving important tissue architecture (Sun et al., 2021).

MALDI-MSI utilizes robotic precision micro-movement coupled to high powered argon laser for the spatial profiling of both organic and biological matter (Cornett et al., 2007; Stanback et al., 2021). It is capable of high sampling aptitude with the ability to record tens of thousands of pixels from a routine histopathology slide at near single-cell resolution (Andres et al., 2020; Li et al., 2000; Walch et al., 2008). The end result is a multidimensional information-rich dataset containing phenotypic features such as lipids, proteins, and complex carbohydrates (Buck et al., 2017; Stanback et al., 2021). Advantages of MALDI-MSI include 1) direct *in situ* tissue sampling that bypasses lengthy and potentially destructive cell dissociation and isolation protocols, 2) the ability to sample FFPE tissue blocks vastly expanding the capability to test most major human clinical specimens stored in biospecimen facilities across the country, 3) offering near single-cell resolution without complex sample preparation and time intensive sequencing steps, and

4) highly accurate X-Y coordinate/spatial information for each laser shot/pixel. Machine learning analysis of MALDI-MSI data would offers true spatial high-dimensional clustering reduction (HDR) as each clustered MALDI-MSI pixel can be bioinformatically mapped back to tissue architecture with high precision (Ding et al., 2002). To this end, machine learning based spatial HDR has not been applied to MALDI-MSI of complex carbohydrates.

FFPE human tissues are the most readily accessible form of samples available for clinical research (Shi et al., 1991). Direct assessment of spatial metabolism within histopathology from clinical specimens remains one of the most challenging tasks to date, and a major barrier for translation research and discovery of clinical actionable approaches (Li et al., 2007). In this study, we test the hypothesis that unsupervised spatial HDR clustering of complex carbohydrate MALDI-MSI data can dissect tissue heterogeneity and disease histopathology while simultaneously uncovering regional perturbations in metabolism in normal and diseased human FFPE tissue samples. Herein, we report the high-dimensional Metabolomics-Assisted Digital pathology Imaging (Madi) workflow. Madi accurately illuminates tissue heterogeneity and histopathology from both normal and diseased human FFPE clinical specimens. Further, targeted metabolism assessments suggest dysregulation of glycogen or N-linked glycan metabolism maybe one of the underpinnings for the development and progression of key pathology features in respiratory diseases such IPF and COVID-19 pulmonary pneumonia.

DESIGN:

Multidimensional nature of MALDI-MSI datasets.

MALDI-MSI is an emerging technology to study molecular features at near single-cell resolution (Amantonico et al., 2010). Biological samples are coated with an ionization matrix to improve excitability upon laser desorption ionization. Each laser ablation spot is registered as a pixel and each pixel is registered with a X-Y coordinate with precision and accuracy (Andres et al., 2020; Stanback et al., 2021). Anabolic pathways for complex carbohydrates such as glycogen and N-linked glycans are critical but vastly understudied facets of glucose metabolism. Moreover, N-linked glycans and glycogen are metabolically channeled through common substrates (Patel et al., 2014; Sun et al., 2021). Comprehensive profiling of both can elucidate compartmentalized metabolism of how glucose is utilized within a cell (Fig. 1A). Recently, a technique was developed for the multiplexed imaging of N-linked glycans and glycogen using MALDI-MSI (Fig. 1B) (Sun et al., 2021). This method takes advantage of two highly specific enzymes, isoamylase and peptide: N-glycosidase F (PNGaseF) F that cleaves glycogen to free linear oligosaccharide chains and release free N-linked glycans from proteins, respectively. Subsequently, linear oligosaccharides and N-glycans can be distinguished by ion mobility separation during MALDI-MSI (Fig. S1) (Sun et al., 2021).

Multi-dimensional nature of MALDI-MSI datasets is highlighted by the fact that each pixel from a MALDI-MSI experiment contains a full ion spectrum of molecular features detected (Fig. 1C). MALDI-MSI datasets can be visualized by selecting individual *m/z* from the combine total ion current (TIC) to generate a heatmap of all recorded pixels (Fig. 1D). To demonstrate the multi-dimensional complexity of MALDI-MSI datasets, we performed N-linked glycan and glycogen multiplexed imaging using a human liver section without adverse histopathology. Based on the

combined TIC over the entire tissue, we can identify complex carbohydrate *m/z* with distinct spatial distribution within the liver section. Conversely, we can extract complex carbohydrate features from each pixel recorded by MALDI-MSI (Fig. 1E).

High dimensional clustering of MALDI-MSI datasets.

To further explore the full potential of the multiplexed MALDI-MSI workflow, we developed Madi, a tool that takes advantage of the biological significance of complex carbohydrates and high-dimensional nature of MALDI-MSI datasets to study tissue anatomy and biology. There are two main modules of Madi: first, user input of curated MALDI-MSI datasets and second, machine learning of randomized clustering and spatial mapping (Fig. 2A). For the user input module, comprehensive *m/z* integration is required to account for mass drift during the sample run time, this step is critical to boost *m/z* intensity and MALDI image quality (Fig. S2A and B). A carefully curated list of 50*m/z* MALDI matrix peaks and 208 glycogen and N-linked glycans *m/z* were selected to assist in the machine learning process, aiding in noise reduction and improved normalization (table S1). The curated data is exported as tabular format for the machine learning module.

For the machine learning module, Madi first performs normalization of complex carbohydrate features through TIC (Fig. 2B). Normalized datasets undergo un-supervised location agnostic dimensionality reduction and clustering using uniform manifold approximation and projection (UMAP). Spatial distribution of unique complex carbohydrate features and their UMAP cluster locations are shown in Figure 2C and S2C. The final step is spatial extrapolation of UMAP clusters based on pixel coordinates to reveal spatial regions of interests (Fig. 2D). As an optional step, Madi can accurately identify spatial CHCA matrix clusters and omit it from the final spatial cluster plot (Fig. 2E and F). Spatial clusters can now be matched to histopathology analysis and interesting regions can further be examined by differential abundance and pathway enrichment analyses.

RESULTS

Madi analysis of normal human organs.

The human liver is a metabolic hub responsible for carbohydrate conversation and maintaining blood glucose levels (Rui, 2011). Liver tissue architecture includes sheets of hepatocytes that form liver lobules with interwoven blood vessels, mainly portal veins (Sasse et al., 1992). Hepatocytes within the liver lobule are the site of glycogen metabolism and glucose release (Ferrer et al., 2003). To test whether Madi spatial clusters match to liver tissue architecture and structures, we performed detailed histology analysis using an adjacent liver section stained with hematoxylin and eosin (H&E) stain followed by annotation by a panel of four expert clinical pathologists at the University of Kentucky. Madi identified 18 unique clusters within the liver section based on unsupervised UMAP clustering (Fig. 3A-B). By matching to histology assessments, Madi accurately identified liver structures such as liver lobules, smooth muscles, and portal veins (Fig. 3C-E). More interestingly, Madi identified an inner and outer layer within the liver lobule (cluster 6 and 7) and separated both longitudinal and cross cut sections of the portal vein (cluster 0 and 12; Fig. 3C-E). Targeted analyses of overrepresented complex carbohydrates among each cluster revealed molecular features supported by current known

literature (Fig. 3F). For example, liver lobules are enriched for glycogen features, smooth muscle regions show high-mannose N-linked glycans, and portal veins contain mostly complex N-glycans (Fig. 3G). Histopathology analysis reveal portal vein is filled with blood serum such as monocytes and erythrocytes and possible contributors to the N-linked glycan profile. Finally, we performed glycogen structural analysis between inner and outer liver lobule and portal veins. Glycogen structure is the distribution of linear glucose chains released by enzymatic digestion (Fig. S1A) (Akai et al., 1971; Sun et al., 2021); shorter chains represent outer chains of glycogen and longer chains represent the glycogen core structure (Manners, 1991). As expected the hepatocytes containing liver lobules have both shorter and longer chain length distribution than the portal vein. Inner layer of the lobule has higher short glycogen chain abundance than the outer layer, however there were no differences between longitudinal and cross section portal vein regions (Fig. 3H).

To further validate the application of Madi in normal human tissue structures, we obtained a set of normal (non-dementia diagnosis) matched frontal cortex and hippocampal tissue sections resected from the same individual. Madi analysis highlighted major anatomical regions of the brain (Fig. 3I-J). For the frontal cortex section, brain structures highlighted include grey and white matter track of the frontal cortex (Fig. 3I-K). In hippocampal section, brain structures identified included the hippocampus, grey matter track, white matter track, and amygdala (Fig. 3K). Glycogen and N-linked glycan features are heterogenous among different regions (Fig. S3A). Recently, a study highlighted the metabolic interplay between glycogen and N-linked glycans and their importance for whole brain function, and dysregulation leads to sever childhood dementia (Sun et al., 2021). Madi analyses highlighted the carbohydrate complexity among different human brain structures, and detailed regional specific analyses are warranted for both normal brain and aging-related dementia patients in the future.

Madi identifies major pathologies from human idiopathic pulmonary fibrosis.

To test whether Madi can identify histopathology from human diseased tissue, we performed MALDI-MSI on two tissue sections from a human IPF patient (ID: A5 and A4, Table S1). IPF is a serious disease with symptoms that include thickening of the alveolar walls from mucin aggregation and uncontrolled myofibroblast growth that lead to fibrosis (Ballester et al., 2019; King Jr et al., 2011). IPF patients suffer poor gas exchange and tissue oxygenation that lead to other co-morbidities (Raghu et al., 2015). Mechanisms driving IPF pathologies are poorly understood due to limited availability of mouse models and human tissues for analysis. Tissue sections were preselected by the presence of unique pathologies within each section. Madi identified 16 and 21 unique spatial clusters, respectively, between each tissue section (Fig. 4A and B and S4A and B). Spatial clusters were matched to expert histopathology assessment of the adjacent tissue stained with H&E. Spatial clusters matched accurately to end stage fibrosis, mucin aggregates in the airway, diffuse alveolar damage (DAD), edematous loose stroma, and smooth muscles of the lung in sample A5 (Fig. 4C-E), and to proteinaceous fluid, edematous loose stroma, chronic inflammation, and end stage fibrosis in tissue A4 from the same patient resected from a different lobe of the lung (Fig. S4 C-E).

For a more in depth analysis of IPF pathologies, we highlighted the overrepresented carbohydrate features in DAD, mucin, and end stage fibrosis in sample A5 (Fig. 4D); and end stage fibrosis with edematous loose stroma in sample A4 (Fig. S4D) to demonstrate unique over-expressed N-linked glycans correlated well spatially with distinct pathologies (Fig. 4F and S4F). Finally, we performed pathway enrichment analysis based on over-represented N-glycans and glycogen features for end stage fibrosis and mucin aggregates, both of which are common pathologies and primary drivers of IPF clinical course (Ballester et al., 2019; Lynch et al., 2005). End stage fibrosis is enriched for complex biantennary N-linked glycans with terminal galactose, fucose, and/or sialic acids modifications. The biosynthesis of complex biantennary N-glycans occurs at the medial to trans Golgi (Reily et al., 2019). More interestingly, galactose addition in N-linked glycans and glycogen biosynthesis shares the metabolite UDP-glucose as the rate-limiting substrate (Fig. 4H). To our surprise, we found glycogen as the most highlighted molecular feature of mucin aggregates (Fig. 4H). The molecular composition of mucin aggregates has not yet been reported; however, mucin aggregates are highlighted by Periodic acid-Schiff (PAS) staining during histopathology analysis, a common stain that also used to detect glycogen as well (Gollnick et al., 1973). These results are intriguing and serve as basis for further studies on the molecular and metabolic drivers of different IPF pathologies.

Madi identified major pathologies in human COVID-19 pneumonia.

Coronavirus disease 2019 (COVID-19), caused by severe acute respiratory syndrome coronavirus 2 (SARS-CoV-2), has led to the current global pandemic and poses significant health risk for individuals who are 65 older. Rapid advancement in our understanding of COVID-19 disease progression highlighted the importance of N-linked glycans in the clinical course of the disease (Montefusco et al., 2021; Watanabe et al., 2020; Wentworth and Holmes, 2001); however, detailed mechanistic insight into disease progression remains a critical knowledge gap in the field. To test whether Madi can reveal fundamental changes in N-linked glycan metabolism associated with COVID-19 pneumonia, we obtained terminal human lung tissue with COVID-19 pneumonia from two separate lobes of the same patient (Fig. 5A). Madi identified 14 and 13 unique spatial clusters between the two tissue sections (ID: A43 and A42, Table S1, Fig. S5A-D). Spatial clusters were matched to expert histopathology assessment of the adjacent tissue stained with H&E (Fig 5B-F). In sample A43, Madi accurately identified DAD, early-, intermediate-, and end-stage fibrosis, and DAD; while in sample A42, spatial clusters identified were acute fibrinous and organizing pneumonia (AFOP), arteries, edematous loose connective tissue, and lung parenchyma with chronic inflammation and pulmonary alveolar macrophages (Fig. 5F, S5E-H).

We highlighted the overrepresented carbohydrate features in DAD, fibrosis, and mucin in sample A43 (Fig. S5I), and AFOP and late-stage fibrosis in sample A42 (Fig. S5J), to demonstrate unique over-expressed N-linked glycans that correlate spatially with distinct COVID-19 pathologies (Fig. S5K,L). Since AFOP and DAD are two if the major pathologies that are associated with negative prognosis of COVID-19 (de Almeida Monteiro et al., 2021; Flikweert et al., 2020; Polak et al., 2020), we performed pathway enrichment analysis in these two distinct histopathological regions (Fig. 5G). In DAD, overrepresented N-linked glycans included complex bisecting and branched N-glycans with terminal galactose, fucose, and sialic acid modifications

(Fig. 5H). These glycans are synthesized in the trans Golgi through step wise addition from biantennary N-linked glycans (Reily et al., 2019). Conversely, high-mannose N-glycans are the major N-glycans expressed in AFOP regions (Fig. 5I). High mannose N-glycan biosynthesis occurs in the ER and cis Golgi, as a direct extension of glucose utilization but also share common substrate, glycogen biosynthesis. Increased high-mannose N-glycans is indictive of aberrant ER metabolism from either over production of UDP-mannose or lack of enzymatic trimming required for N-linked glycan maturation to proceed to the trans Golgi (Bieberich, 2014). Collectively, Madi highlighted fundamental changes in N-linked glycan metabolism associated with COVID-19 pneumonia.

Madi reveals lung fibrosis shares common N-linked glycan features.

Lung fibrosis is caused by the uncontrolled growth of myofibroblast and a major disease pathology associated with poor prognosis in acute respiratory distress syndrome (ARDS) (Martin et al., 1995). In our study, Madi identified fibrosis in all four lung disease sections tested. We hypothesize that lung fibrosis shares common carbohydrate features between different IPF and COVID-19 tissue sections. To test this hypothesis, we performed targeted analysis of fibrotic regions between two IPF and two COVID-19 sections (Fig. 6A). As expected, complex biantennary N-linked glycans are overrepresented in all four fibrotic sections (Fig. 6B). Further, complex glycans: 1809 *m/z*, 1444 *m/z*, 1791 *m/z*, 2122 *m/z*, 2057 *m/z*, and 1793 *m/z* are universally overrepresented in all fibrotic tissue regions (Fig. 6C and D and S6). These results highlight that fibrotic lung tissue from different disease of origin share common molecular features. Collectively, these data also demonstrate the accuracy and consistency of Madi to identify the same tissue pathology among different diseases.

DISCUSSION:

In this study, we developed Madi, a new tool to uncover tissue anatomy, histopathology, and metabolism. Major innovations from our study include the ability to utilize FFPE human clinical samples and simultaneously uncover anatomical /histopathological regions and their metabolism. This tool is developed based on the hypothesis that anabolic complex carbohydrate biosynthetic pathways are critical components of cellular function and tissue structural integrity. We developed this workflow using a normal human liver specimen with well-defined regions of hepatocyte plates with interwoven blood vessels. Madi accurately defines regions of high and low glycogen within liver lobules and portal veins in the liver tissue. We then validated our approach in human brain frontal cortical and hippocampus tissues. Finally, we tested Madi on human diseased lung tissues from IPF and COVID-19 pulmonary pneumonia specimens. Madi identified major histopathology features such as honeycombing, DAD, early/mid/late-stage fibrosis, and AFOP with high precision and accuracy. Collectively, these data highlight the potential application of Madi in future of digital pathology as a tool to potentially accelerate histopathological assessment for disease diagnosis.

Madi utilizes datasets from multiplexed MALDI-MSI of glycogen and N-linked glycans, two critical classes of complex carbohydrates involved in bioenergetics and protein structure function. This high dimensional dataset is similar to the scRNAseq format (Saliba et al., 2014), where complex carbohydrates are biological features stored within each pixel, similar to gene

expression levels within each cell. However, there are many stark differences. First, each pixel from MALDI-MSI is recorded with precision X-Y coordinates to allow true spatial mapping of tissue architecture. Second, multiplexed glycogen and N-linked glycan MALDI-MSI takes advantage of the world largest collection of well-annotated human clinical specimens with decades of clinical course metadata in the form of FFPE. The ability to utilize FFPE tissue also bypasses the need to collect fresh tissue from surgery for human clinical studies. The *in situ* nature of MALDI-MSI also avoids lengthy and potentially destructive cell isolation steps, preserving tissue architecture. Of note, many histopathological features such as late-stage fibrosis and mucin patches contain large fractions of non-cellular features, i.e., mucin patches are aggregation of glycosylated proteins. These features are often lost in single-cell analyses but are preserved by the MALDI-MSI workflow. To this end, Madi is not designed to replace scRNAseq workflow; we speculate and anticipate that Madi would work in synergy with scRNAseq analysis in the future.

Another advantage of Madi is the ability to map metabolism in unique anatomical or histopathological regions. Metabolism has been shown to be a promising target for precision medicine (Nielsen, 2017); however, animal models that phenocopy unique human lung pathologies require further development (Carrington et al., 2018). Therefore, the inability to tease out *in situ* human lung metabolism is a major barrier in the development of targeted therapeutics for idiopathic lung fibrosis. Madi can identify pathological regions and reveal altered metabolism within these regions. In our analysis, complex N-linked glycans are highly expressed in late-stage fibrotic tissue of an IPF patient. In fibrosis, overrepresented complex carbohydrates belong to complex biantennary N-linked glycans containing either a fucose or/and sialic acid modifications. Fucosylation and sialylation occur in the Golgi and ultimately become terminal cell surface modifications through vesicle trafficking (Reily et al., 2019). Cells utilize fucose and sialic acid modifications on surface receptors or structural proteins to modulate communication, migration, and intracellular signaling (Li et al., 2018; Schauer, 1985). Both fucosylation and sialylation have been reported to modulate signaling pathways for myofibroblast differentiation and proliferation (Sasaki et al., 2017; Sun et al., 2017). Another common pathology recognized IPF is mucin aggregates within the thickened airways. Using Madi, we found mucin aggregates contain high levels of glycogen in IPF patient tissue. This data is intriguing, as extracellular glycogen has not been reported, nor has it been reported as a structural component of mucin. The mechanisms behind glycogen accumulation and trafficking in mucin aggregates during IPF warrant future investigation.

In 2019, the novel coronavirus disease (COVID-19) caused by severe acute respiratory syndrome (SARS) CoV-2 rapidly became a global pandemic and swept through nations due to its high rate of transmission. COVID-19 pneumonia has been leading cause of mortality in individual infected with SARS CoV-2, and core pathologies such as AFOP and DAD are frequently identified in COVID-19 patients with rapidly deteriorating health (de Almeida Monteiro et al., 2021; Flikweert et al., 2020; Polak et al., 2020). Recently, a growing body of evidence suggest N-linked glycosylation is key for viral entry through the ACE2 receptor (Mehdipour and Hummer, 2021; Zhao et al., 2020). Further, there are fundamental shifts in complex carbohydrate metabolism, especially N-linked glycans, based on serum analysis of patients during the course

of SARS CoV-2 infection (Montefusco et al., 2021). Madi analysis of AFOP and DAD in COVID-19 pneumonia showed unique metabolic features between these two pathological regions. Interestingly, high-mannose N-linked glycans are highly expressed in AFOP tissues from COVID-19 patients. Increased high-mannose N-linked glycans represent a defect in the trimming of N-linked glycan precursors and prevent proper oligomerization and branching. As a result, improperly processed high-mannose N-linked glycans are concentrated at the membrane. High mannose N-linked glycans have been identified in cancer and COPD, and they are hypothesized to disrupt cell-to-cell communication and facilitate uncontrolled cellular proliferation. Further, high-mannose N-glycans are well known immune modulators. Increased high-mannose N-glycan may be one of the factors driving the cytokine storm (Vaninov, 2020), one of the major causes of COVID-19 related mortality. Collectively, our results support the notion of fundamental changes in N-linked glycosylation in host tissue during SARS CoV-2 infection.

LIMITATIONS AND FUTURE DIRECTIONS

In study, we describe a new tool for digital pathology imaging to study underlying metabolic perturbations in human clinical samples. One limitation of this study is due to the nature of human clinical specimens, age and sex matched normal tissue is challenging to acquire. Results from our study should be tested in appropriate mouse models with age and sex matched normal tissue. Due to limitations of our MALDI-MSI instrument, we performed the analysis with a step size of 75μm and focused anatomical and histopathological regions on tissue sections. Some MALDI MSI instruments are now capable of subcellular imaging. Finally, there are undefined clusters with unique anatomical distribution. Future studies should include integration of Madi with other next-generation imaging tools such as multiplexed ion beam imaging (MIBI), co-detection by indexing (CODEX), and scRNAseq to allow comprehensive single-cell genotype to phenotype analysis and characterize additional undefined clusters.

Acknowledgments

We would like to thank Dr. Vander Kooi and Gentry lab members for vigorous discussions regarding the work, Mrs. Dana Napier for performing histo-staining on tissue slices, and the Markey Cancer Center.

Author Contributions

Conceptualization, R.C.S. Methodology, R.C.S., and J.L.; Investigation, L.R.C., D.B.A., Q.S., T.R.H., R.C.S, L.E.A.Y, J.E.F., A.V.H., R.J.M., K.J.A., W.J.A., C.M.W., and H.A.C., Writing – Original Draft, R.C.S.; Writing – Review & Editing, R.C.S., L.R.C., W.J.A., C.M.W., and D.B.A.; Funding Acquisition, R.C.S. Resources, R.C.S.; Supervision, R.C.S.

Funding

This study was supported by National Institute of Health (NIH) grants R01 AG066653, St Baldrick's Career Development Award, V-Scholar Grant, Rally Foundation Independent Investigator Grant to R.C.S., and L.R.C was supported by NIH/NCI training grant T32CA165990. National Institute of Health (NIH) grants R01 R21NS121966 to W.J.A. This research was also supported by funding from the University of Kentucky Markey Cancer Center and the NIH-

funded Biospecimen Procurement & Translational Pathology Shared Resource Facility of the University of Kentucky Markey Cancer Center P30CA177558.

Conflict of Interests

R.C.S. has research support and received consultancy fee from Maze Therapeutics. D.B.A. received book royalty from Wolters Kluwer. R.C.S. is a co-founder of Attrogen LLC.

REFERENCES

Akai, H., Yokobayashi, K., Misaki, A., and Harada, T. (1971). Complete hydrolysis of branching linkages in glycogen by Pseudomonas isoamylase: distribution of linear chains. Biochimica et Biophysica Acta (BBA)-General Subjects *237*, 422-429.

Amantonico, A., Urban, P.L., Fagerer, S.R., Balabin, R.M., and Zenobi, R. (2010). Single-cell MALDI-MS as an analytical tool for studying intrapopulation metabolic heterogeneity of unicellular organisms. Analytical chemistry *82*, 7394-7400.

Andres, D.A., Young, L.E., Gentry, M.S., and Sun, R.C. (2020). Spatial profiling of gangliosides in mouse brain by mass spectrometry imaging. Journal of lipid research *61*, 1537.

Ballester, B., Milara, J., and Cortijo, J. (2019). Mucins as a new frontier in pulmonary fibrosis. Journal of clinical medicine *8*, 1447.

Bieberich, E. (2014). Synthesis, processing, and function of N-glycans in N-glycoproteins. In Glycobiology of the nervous system (Springer), pp. 47-70.

Buck, A., Aichler, M., Huber, K., and Walch, A. (2017). In situ metabolomics in cancer by mass spectrometry imaging. Advances in cancer research *134*, 117-132.

Carrington, R., Jordan, S., Pitchford, S.C., and Page, C.P. (2018). Use of animal models in IPF research. Pulmonary Pharmacology & Therapeutics *51*, 73-78.

Cornett, D.S., Reyzer, M.L., Chaurand, P., and Caprioli, R.M. (2007). MALDI imaging mass spectrometry: molecular snapshots of biochemical systems. Nature methods *4*, 828-833.

de Almeida Monteiro, R.A., Duarte-Neto, A.N., da Silva, L.F.F., de Oliveira, E.P., do Nascimento, E.C.T., Mauad, T., do Nascimento Saldiva, P.H., and Dolhnikoff, M. (2021). Ultrasound assessment of pulmonary fibroproliferative changes in severe COVID-19: a quantitative correlation study with histopathological findings. Intensive care medicine *47*, 199-207.

Ding, C., He, X., Zha, H., and Simon, H.D. (2002). Adaptive dimension reduction for clustering high dimensional data. In 2002 IEEE International Conference on Data Mining, 2002. Proceedings. (IEEE), pp. 147-154.

Ferrer, J.C., Favre, C., Gomis, R.R., Fernández-Novell, J.M., García-Rocha, M., de la Iglesia, N., Cid, E., and Guinovart, J.J. (2003). Control of glycogen deposition. FEBS letters *546*, 127-132.

Flikweert, A.W., Grootenboers, M.J., Yick, D.C., du Mée, A.W., van der Meer, N.J., Rettig, T.C., and Kant, M.K. (2020). Late histopathologic characteristics of critically ill COVID-19 patients: Different phenotypes without evidence of invasive aspergillosis, a case series. Journal of critical care *59*, 149-155.

Gollnick, P., Armstrong, R., Sembrowich, W., Shepherd, R., and Saltin, B. (1973). Glycogen depletion pattern in human skeletal muscle fibers after heavy exercise. Journal of Applied Physiology *34*, 615-618.

Gu, J., Isaji, T., Xu, Q., Kariya, Y., Gu, W., Fukuda, T., and Du, Y. (2012). Potential roles of N-glycosylation in cell adhesion. Glycoconjugate journal *29*, 599-607.

Islam, S., Zeisel, A., Joost, S., La Manno, G., Zajac, P., Kasper, M., Lönnerberg, P., and Linnarsson, S. (2014). Quantitative single-cell RNA-seq with unique molecular identifiers. Nature methods *11*, 163.

King Jr, T.E., Pardo, A., and Selman, M. (2011). Idiopathic pulmonary fibrosis. The Lancet *378*, 1949-1961.

Li, J., Hsu, H.-C., Mountz, J.D., and Allen, J.G. (2018). Unmasking Fucosylation: from Cell Adhesion to Immune System Regulation and Diseases. Cell Chemical Biology *25*, 499-512.

Li, J., Smyth, P., Flavin, R., Cahill, S., Denning, K., Aherne, S., Guenther, S.M., O'Leary, J.J., and Sheils, O. (2007). Comparison of miRNA expression patterns using total RNA extracted from matched samples of formalin-fixed paraffin-embedded (FFPE) cells and snap frozen cells. BMC biotechnology *7*, 1-6.

Li, L., Garden, R.W., and Sweedler, J.V. (2000). Single-cell MALDI: a new tool for direct peptide profiling. Trends in biotechnology *18*, 151-160.

Liwosz, A., Lei, T., and Kukuruzinska, M.A. (2006). N-glycosylation affects the molecular organization and stability of E-cadherin junctions. Journal of Biological Chemistry *281*, 23138-23149.

Lynch, D.A., Godwin, J.D., Safrin, S., Starko, K.M., Hormel, P., Brown, K.K., Raghu, G., King Jr, T.E., Bradford, W.Z., and Schwartz, D.A. (2005). High-resolution computed tomography in idiopathic pulmonary fibrosis: diagnosis and prognosis. American journal of respiratory and critical care medicine *172*, 488-493.

Manners, D.J. (1991). Recent developments in our understanding of glycogen structure. Carbohydrate polymers *16*, 37-82.

Martin, C., Papazian, L., Payan, M.-J., Saux, P., and Gouin, F. (1995). Pulmonary Fibrosis Correlates With Outcome in Adult Respiratory Distress Syndrome: A Study in Mechanically Ventilated Patients. Chest *107*, 196-200.

Mehdipour, A.R., and Hummer, G. (2021). Dual nature of human ACE2 glycosylation in binding to SARS-CoV-2 spike. Proceedings of the National Academy of Sciences *118*, e2100425118.

Montefusco, L., Nasr, M.B., D'Addio, F., Loretelli, C., Rossi, A., Pastore, I., Daniele, G., Abdelsalam, A., Maestroni, A., and Dell'Acqua, M. (2021). Acute and long-term disruption of glycometabolic control after SARS-CoV-2 infection. Nature Metabolism, 1-12.

Nielsen, J. (2017). Systems Biology of Metabolism: A Driver for Developing Personalized and Precision Medicine. Cell Metabolism *25*, 572-579.

Patel, A.P., Tirosh, I., Trombetta, J.J., Shalek, A.K., Gillespie, S.M., Wakimoto, H., Cahill, D.P., Nahed, B.V., Curry, W.T., and Martuza, R.L. (2014). Single-cell RNA-seq highlights intratumoral heterogeneity in primary glioblastoma. Science *344*, 1396-1401.

Polak, S.B., Van Gool, I.C., Cohen, D., Jan, H., and van Paassen, J. (2020). A systematic review of pathological findings in COVID-19: a pathophysiological timeline and possible mechanisms of disease progression. Modern Pathology *33*, 2128-2138.

Raghu, G., Amatto, V.C., Behr, J., and Stowasser, S. (2015). Comorbidities in idiopathic pulmonary fibrosis patients: a systematic literature review. European Respiratory Journal *46*, 1113-1130.

Reily, C., Stewart, T.J., Renfrow, M.B., and Novak, J. (2019). Glycosylation in health and disease. Nature Reviews Nephrology *15*, 346-366.

Rudd, P.M., Wormald, M.R., Stanfield, R.L., Huang, M., Mattsson, N., Speir, J.A., DiGennaro, J.A., Fetrow, J.S., Dwek, R.A., and Wilson, I.A. (1999). Roles for glycosylation of cell surface receptors involved in cellular immune recognition. Journal of molecular biology *293*, 351-366.
Rui, L. (2011). Energy metabolism in the liver. Comprehensive physiology *4*, 177-197.
Saliba, A.-E., Westermann, A.J., Gorski, S.A., and Vogel, J. (2014). Single-cell RNA-seq: advances and future challenges. Nucleic acids research *42*, 8845-8860.
Sasaki, N., Itakura, Y., and Toyoda, M. (2017). Sialylation regulates myofibroblast differentiation of human skin fibroblasts. Stem Cell Research & Therapy *8*, 81.
Sasse, D., Spornitz, U.M., and Maly, I.P. (1992). Liver architecture. Enzyme *46*, 8-8.
Schauer, R. (1985). Sialic acids and their role as biological masks. Trends in Biochemical Sciences *10*, 357-360.
Shi, S.-R., Key, M.E., and Kalra, K.L. (1991). Antigen retrieval in formalin-fixed, paraffin-embedded tissues: an enhancement method for immunohistochemical staining based on microwave oven heating of tissue sections. Journal of Histochemistry & Cytochemistry *39*, 741-748.
Stanback, A.E., Conroy, L.R., Young, L.E., Hawkinson, T.R., Markussen, K.H., Clarke, H.A., Allison, D.B., and Sun, R.C. (2021). Regional N-glycan and lipid analysis from tissues using MALDI-mass spectrometry imaging. STAR protocols *2*, 100304.
Stanley, P., Taniguchi, N., and Aebi, M. (2017). N-glycans. Essentials of Glycobiology [Internet]. 3rd edition.
Sun, R.C., Young, L.E., Bruntz, R.C., Markussen, K.H., Zhou, Z., Conroy, L.R., Hawkinson, T.R., Clarke, H.A., Stanback, A.E., and Macedo, J.K. (2021). Brain glycogen serves as a critical glucosamine cache required for protein glycosylation. Cell Metabolism.
Sun, W., Tang, H., Gao, L., Sun, X., Liu, J., Wang, W., Wu, T., and Lin, H. (2017). Mechanisms of pulmonary fibrosis induced by core fucosylation in pericytes. The International Journal of Biochemistry & Cell Biology *88*, 44-54.
Vaninov, N. (2020). In the eye of the COVID-19 cytokine storm. Nature Reviews Immunology *20*, 277-277.
Walch, A., Rauser, S., Deininger, S.-O., and Höfler, H. (2008). MALDI imaging mass spectrometry for direct tissue analysis: a new frontier for molecular histology. Histochemistry and cell biology *130*, 421-434.
Watanabe, Y., Berndsen, Z.T., Raghwani, J., Seabright, G.E., Allen, J.D., Pybus, O.G., McLellan, J.S., Wilson, I.A., Bowden, T.A., and Ward, A.B. (2020). Vulnerabilities in coronavirus glycan shields despite extensive glycosylation. Nature communications *11*, 1-10.
Wentworth, D.E., and Holmes, K.V. (2001). Molecular determinants of species specificity in the coronavirus receptor aminopeptidase N (CD13): influence of N-linked glycosylation. Journal of virology *75*, 9741-9752.
Yan, A., and Lennarz, W.J. (2005). Unraveling the mechanism of protein N-glycosylation. Journal of Biological Chemistry *280*, 3121-3124.
Zenobi, R. (2013). Single-cell metabolomics: analytical and biological perspectives. Science *342*.
Zhao, P., Praissman, J.L., Grant, O.C., Cai, Y., Xiao, T., Rosenbalm, K.E., Aoki, K., Kellman, B.P., Bridger, R., Barouch, D.H., et al. (2020). Virus-Receptor Interactions of Glycosylated SARS-CoV-2 Spike and Human ACE2 Receptor. Cell Host & Microbe *28*, 586-601.e586.

Figure 1.

MALDI-MSI of complex carbohydrates is a multidimensional dataset.

(**A**) Simplified representative pathways of glucose utilization inside a cell. Anabolic metabolism of glycogen and N-linked glycans through the ER and Golgi are detected by multiplexed glycogen and N-linked MALDI-MSI.

(**B**) Schematic of the workflow for multiplexed imaging of glycogen and N-glycans using human FFPE specimens. Human FFPE samples sectioned on a microscope slide are co-treated with peptide-N-glycosidase F (PNGase F) to cleave and release N-glycans and isoamylase to cleave α-1,6-glycosidic bonds releasing linear oligosaccharide chains. Following application of α-cyano-4-hydroxycinnamic acid (CHCA) ionization matrix for MALDI, samples were analyzed by MALDI and quadrupole time-of-flight mass spectrometry.

(**C**) Left: Schematic of molecular ions recorded in each pixel after laser desorption ionization. Right: Heatmap of a specific biological feature (*m/z*) extrapolated from total ion current (TIC) after MALDI-MSI of an entire tissue section.

(**D**) TIC representing the sum of all pixels after MALDI-MSI of a human liver section.

(**E**) Spatial heatmap images of selected complex carbohydrate ions (*m/z*) corresponding to either glycogen or N-linked glycans selected from (**D**). *m/z* values and molecular structures of selected oligosaccharide chain and N-linked glycans are on top of the heatmap. An adjacent liver section stained with hematoxylin and eosin (H&E) is presented below the heatmap for 1743 *m/z*.

(**F**) TIC extracted from three unique pixels based on the spatial heatmap presented in (**E**).

Figure 2.

High dimensional reduction and spatially clustering by Madi.

(**A**) Simplified flow chart for the general workflow of Madi. The user input module includes MALDI-MSI and data curation, followed by the machine learning module that utilizes unsupervised UMAP clustering and spatial annotation of unique clusters.

(**B**) Representative input data for machine learning and unsupervised cluster analysis. 5% of total pixels and mixture of matrix and carbohydrate *m/z* were shown as heatmap for ease of visualization.

(**C**) Spatial heatmap of two unique glycogen (1013 *m/z*) and N-linked glycan (1809 *m/z*) (right) and their location within UMAP clusters (left).

(**D**) UMAP clustering followed by spatial annotation of the human liver specimen by Madi analysis.

(**E**) UMAP clustering followed by spatial annotation showing matrix only cluster from the human liver specimen by Madi analysis.

(**F**) UMAP clustering followed by spatial annotation after matrix removal from the human liver specimen shown in (**D**).

Figure 3.

Madi analysis reveal human liver and brain tissue architecture and metabolism.

(A) Hematoxylin and eosin (H&E) staining of an immediate adjacent section used for MALDI-MSI for histopathology assessment.

(**B**) Unsupervised high dimensional reduction (HDR) shown as UMAP clustering (left) and spatial annotation for all identified clusters based on pixel coordinate information.
(**C**) Zoomed in images of H&E stained liver section showing liver lobules, smooth muscle, and portal veins.
(**D**) UMAP clusters and spatial annotation highlighting inner liver lobule (cluster 6), outer liver lobule (cluster 1), smooth muscle (cluster 0), and portal vein (cluster 12).
(**E**) Annotation of spatial clusters to histopathology by four board certified pathologists.
(**F**) Clustering heatmap showing top 10 most highly expressed complex carbohydrate features in inner liver lobule (cluster 6), outer liver lobule (cluster 1), smooth muscle (cluster 0), and portal vein (cluster 12). *M/z* that represent carbohydrate features were shown on the left. *M/z* and corresponding carbohydrate features can be found in **Table S1**.
(**G**) Schematics of liver architecture regions (top) and representative spatial distribution and heatmap of a single carbohydrate feature for each region based on differential expression analysis in (**F**) (bottom). Molecular structure and corresponding *m/z* (rounded to the nearest whole number) of each complex carbohydrate feature were shown above the spatial heatmap.
(**H**) Glycogen chain length abundance and distribution based on UMAP clusters between inner liver lobule (cluster 6), outer liver lobule (cluster 1), smooth muscle (cluster 0), and portal vein (cluster 12).
(I) Hematoxylin and eosin (H&E) staining of an immediate adjacent brain section of frontal cortex and hippocampal regions used for MALDI-MSI.
(**J**) Unsupervised high dimensional reduction (HDR) shown as UMAP clustering for both frontal cortex and hippocampal sections.
(**K**) Spatial annotation for all identified UMAP clusters for both frontal cortex and hippocampal sections based on pixel coordinate information.

Figure 4.
Madi analysis of tissue section from idiopathic pulmonary fibrosis patient (IPF).
(A) Hematoxylin and eosin (H&E) staining of an immediate adjacent IPF section used for MALDI-MSI for histopathology assessment.
(**B**) Unsupervised high dimensional reduction (HDR) shown as UMAP clustering (left) and spatial annotation of all identified cluster based on pixel coordinate information.
(**C**) Zoomed in images of H&E stained IPF section showing mucin aggregates, late-stage fibrosis, and diffuse alveolar damage (DAD).
(**D**) UMAP clustering and spatial annotation highlighting mucin aggregates, late-stage fibrosis, and DAD.
(**E**) Annotation of spatial clusters to histopathology by four board certified pathologists.
(**F**) Clustering heatmap showing top 10 most highly expressed carbohydrate features in mucin aggregates, late-stage fibrosis, and DAD. *M/z* that represent carbohydrate features were shown on the left. *M/z* and corresponding complex carbohydrates can be found in **Table S1**.
(**G**) Representative spatial distribution and heatmap of a single carbohydrate feature for each region based on differential expression analysis in (**F**). Molecular structure and corresponding *m/z* (rounded to the nearest whole number) of each complex carbohydrate feature are shown below.

(**G**) Pathway enrichment analysis based on overrepresented carbohydrate features from (**F**) for late-stage fibrosis and glycogen deposited in mucin aggregated in airways of IPF patients.

Figure 5.
Madi analysis of tissue section from COVID-19 patient
(A) Schematic of Madi analysis of tissue sections from COVID-19 patient.
(B) Hematoxylin and eosin (H&E) staining of an immediate adjacent COVID-19 section used for Madi analysis.
(**C**) UMAP clustering and spatial annotation highlighting mucin aggregates, late-stage fibrosis, and diffuse alveolar damage (DAD) in tissue section resected from lower right lobe.
(D) H&E staining of an immediate adjacent COVID-19 section used for Madi analysis.
(**E**) UMAP clustering and spatial annotation highlighting acute fibrinous and organizing pneumonia (AFOP) and early/late-stage fibrosis in tissue section resected from upper left lobe.
(**F**) Annotation of spatial clusters to histopathology by four board certified pathologists.
(**G**) Zoomed in images of H&E stained sections showing DAD and AFOP.
(**H**) Pathway enrichment analysis based on overrepresented carbohydrate features from (**E**) for DAD in COVID-19 patient section.
(**I**) Pathway enrichment analysis based on overrepresented carbohydrate features from (**E**) for AFOP in COVID-19 patient section.

Figure 6.
Fibrosis from different IPF and COVID-19 tissues share common N-linked glycan features.
(**A**) Zoomed in images of hematoxylin and eosin (H&E) stained tissue sections showing IPF or COVID-19 fibrosis.
(**B**) Zoomed in images of clustering heatmap showing top 10 most highly expressed complex carbohydrates from spatial clusters corresponding to fibrosis in IPF and COVID-19 patient sections based on Madi and histopathology analysis.
(**C**) Molecular structures of six N-linked glycans that are universally overrepresented in all fibrotic regions.
(**D**) Spatial distribution and heatmap of the complex N-glycan 1809 *m/z* in IPF and COVID-19 MALDI-MSI scans highlighting fibrotic regions.

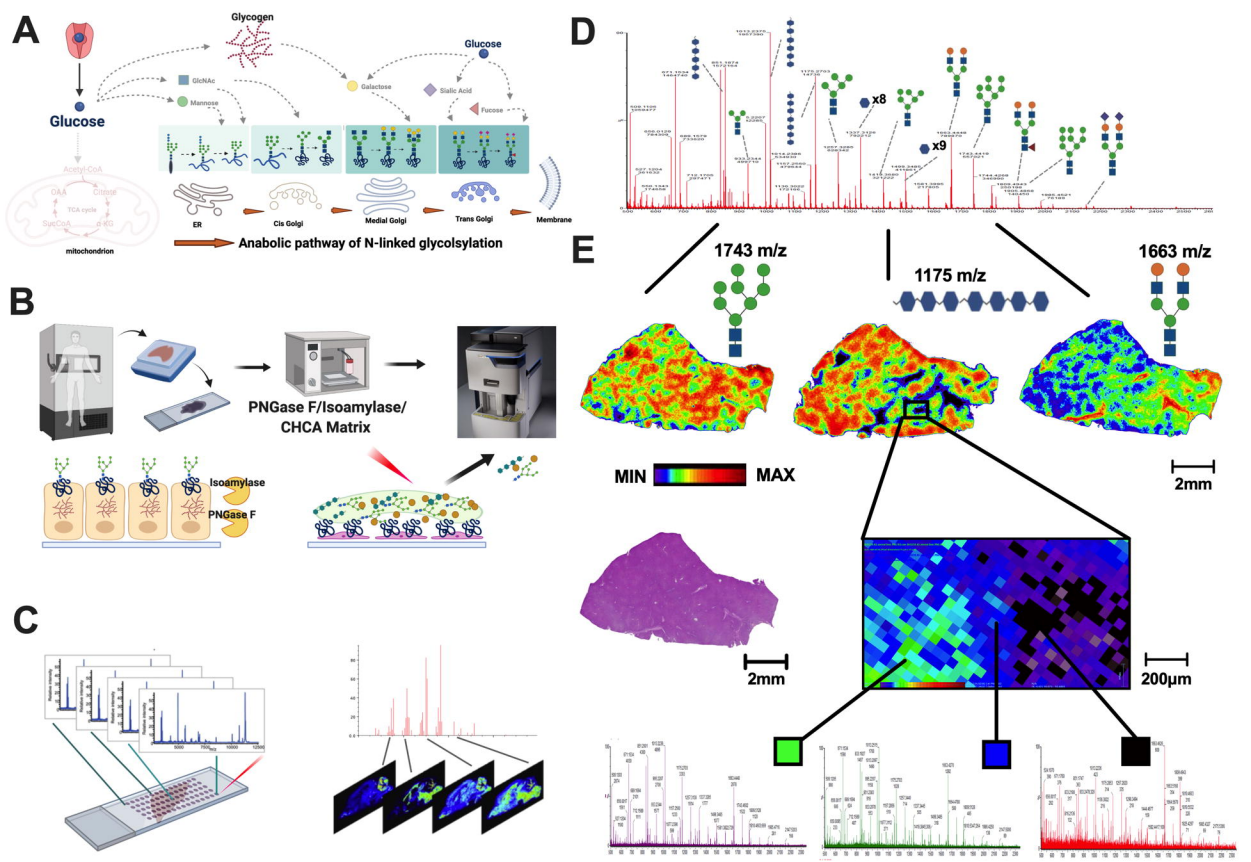
A
Glycogen
Glucose
Glucose
GlcNAc
Galactose
Sialic Acid
Fucose
Mannose
Acetyl-CoA
Citrate
OAA
TCA cycle
Succ-CoA
α-KG
mitochondrion
ER
Cis Golgi
Medial Golgi
Trans Golgi
Membrane
Anabolic pathway of N-linked glycolsylation
B
PNGase F/Isoamylase/
CHCA Matrix
Isoamylase
PNGase F
C
D
x8
x9
E
1743 m/z
1175 m/z
1663 m/z
MIN
MAX
2mm
2mm
200μm

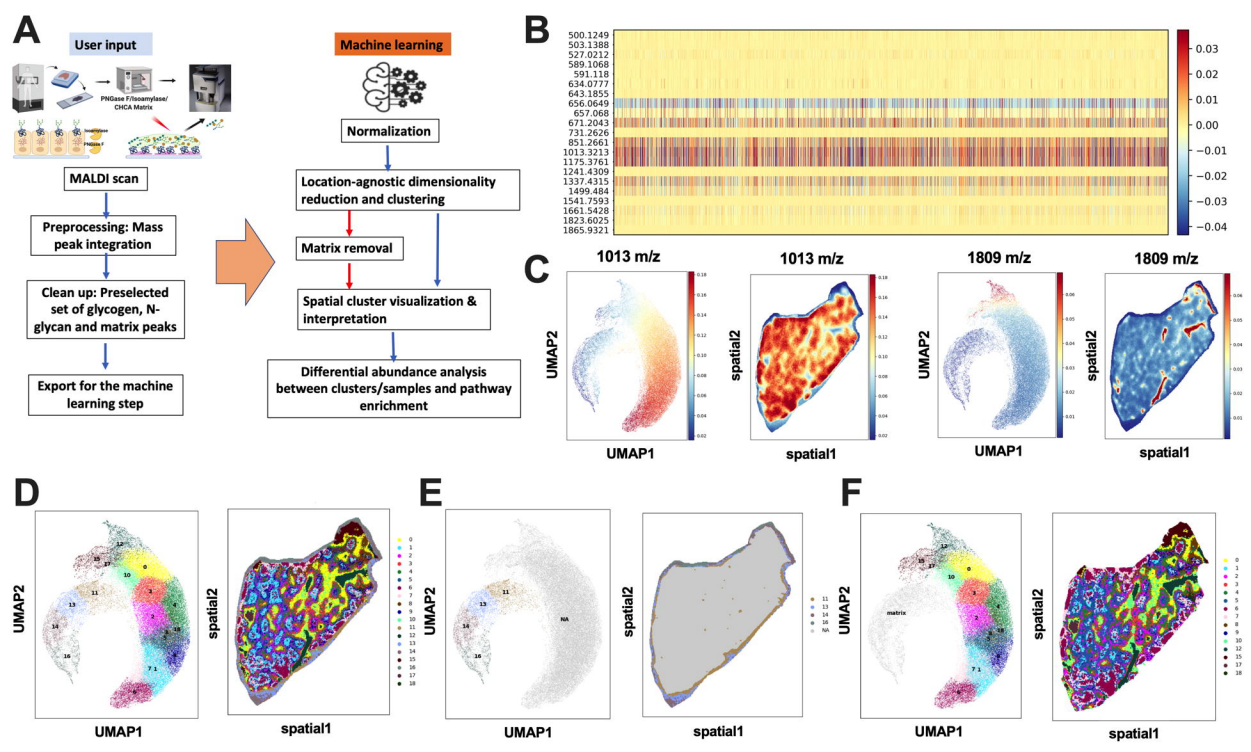
A
User input
PNGase F/Isoamylase/
CHCA Matrix
MALDI scan
Preprocessing: Mass peak integration
Clean up: Preselected set of glycogen, N-glycan and matrix peaks
Export for the machine learning step
Machine learning
Normalization
Location-agnostic dimensionality reduction and clustering
Matrix removal
Spatial cluster visualization & interpretation
Differential abundance analysis between clusters/samples and pathway enrichment
B
500.1249
503.1388
527.0212
589.1068
591.118
634.0777
643.1855
656.0649
657.068
671.2043
731.2626
851.2661
1013.3213
1175.3761
1241.4309
1337.4315
1499.484
1541.7593
1661.5428
1823.6025
1865.9321
0.03
0.02
0.01
0.00
−0.01
−0.02
−0.03
−0.04
C
1013 m/z
1013 m/z
1809 m/z
1809 m/z
UMAP2
UMAP1
spatial2
spatial1
D
E
F
UMAP2
UMAP1
spatial2
spatial1
NA
matrix

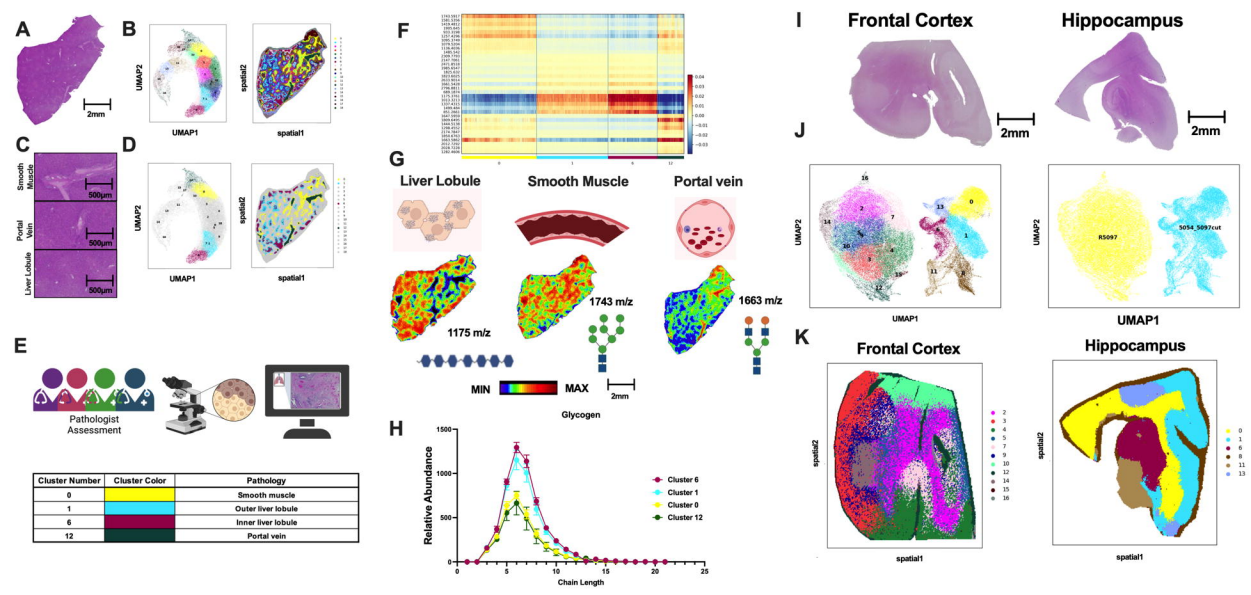

Cluster Number	Cluster Color	Pathology
0		Smooth muscle
1		Outer liver lobule
6		Inner liver lobule
12		Portal vein

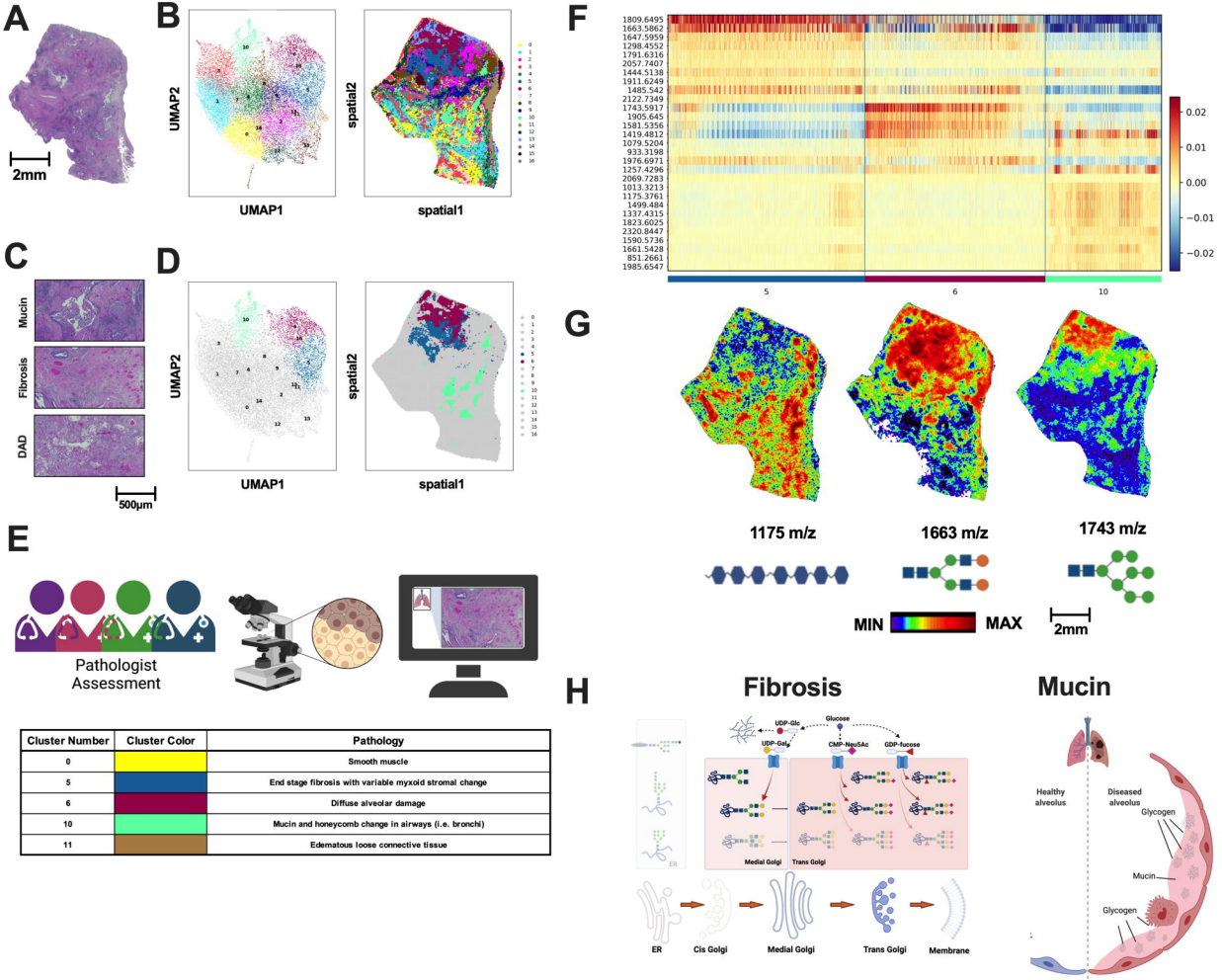

Cluster Number	Cluster Color	Pathology
0		Smooth muscle
5		End stage fibrosis with variable myxoid stromal change
6		Diffuse alveolar damage
10		Mucin and honeycomb change in airways (i.e. bronchi)
11		Edematous loose connective tissue

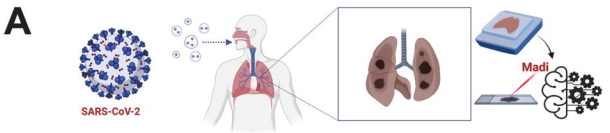

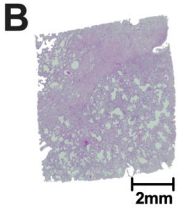

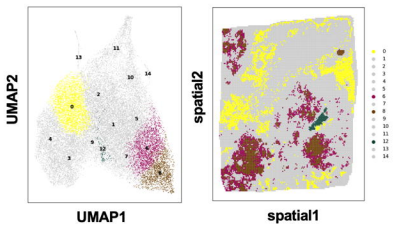

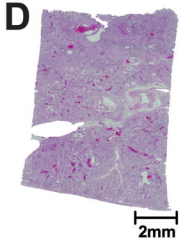

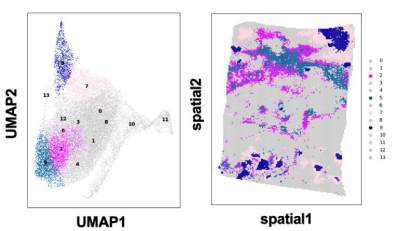

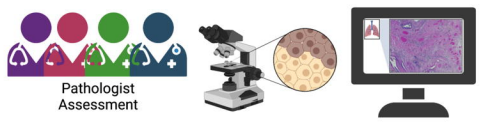

Cluster Number	Cluster Color	Pathology: COVID-19 A43
0		Intermediate stage fibrosis
6		Diffuse alveolar damage
8		Diffuse alveolar damage
12		Mucin

Cluster Number	Cluster Color	Pathology: COVID-19 A42
2		End stage fibrosis with mature collagen deposition and variable myxoid stromal change
5		End stage fibrosis with mature collagen deposition and variable myxoid stromal change
7		Organizing fibrosis immediately adjacent to AFOP
9		Acute fibrinous and organizing pneumonia (AFOP)

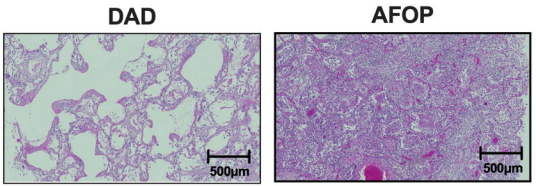

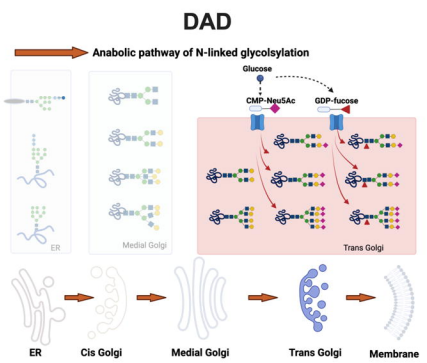

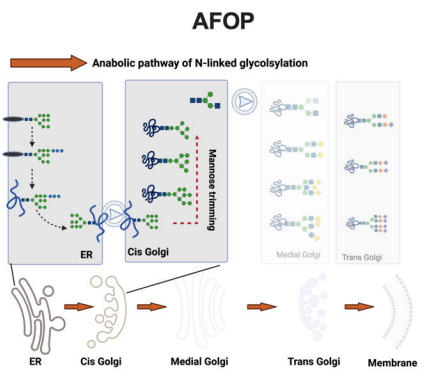

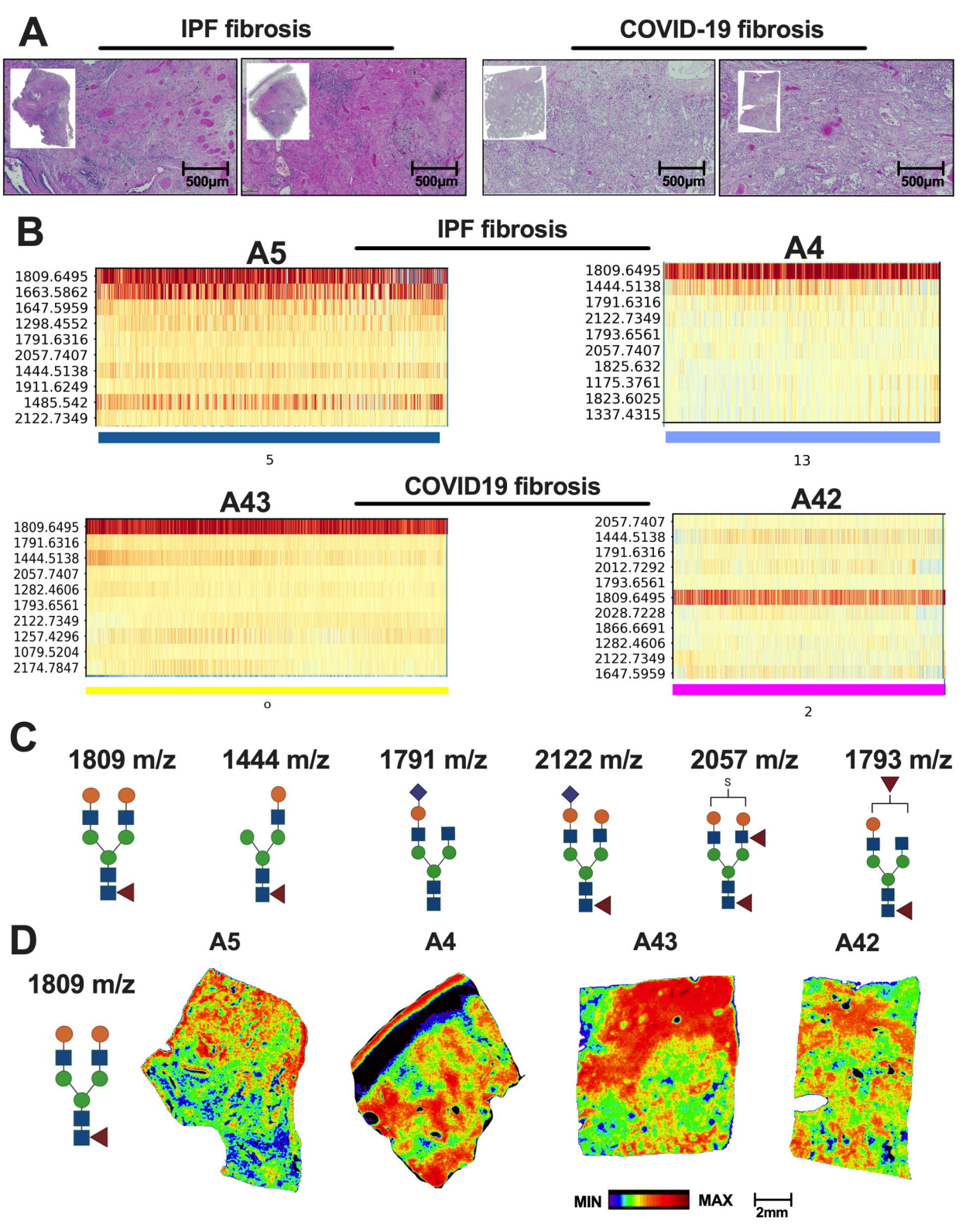
A
IPF fibrosis
COVID-19 fibrosis
500µm
500µm
500µm
500µm
B
IPF fibrosis
A5
1809.6495
1663.5862
1647.5959
1298.4552
1791.6316
2057.7407
1444.5138
1911.6249
1485.542
2122.7349
5
A4
1809.6495
1444.5138
1791.6316
2122.7349
1793.6561
2057.7407
1825.632
1175.3761
1823.6025
1337.4315
13
COVID19 fibrosis
A43
1809.6495
1791.6316
1444.5138
2057.7407
1282.4606
1793.6561
2122.7349
1257.4296
1079.5204
2174.7847
o
A42
2057.7407
1444.5138
1791.6316
2012.7292
1793.6561
1809.6495
2028.7228
1866.6691
1282.4606
2122.7349
1647.5959
2
C
1809 m/z
1444 m/z
1791 m/z
2122 m/z
2057 m/z
S
1793 m/z
D
1809 m/z
A5
A4
A43
A42
MIN
MAX
2mm

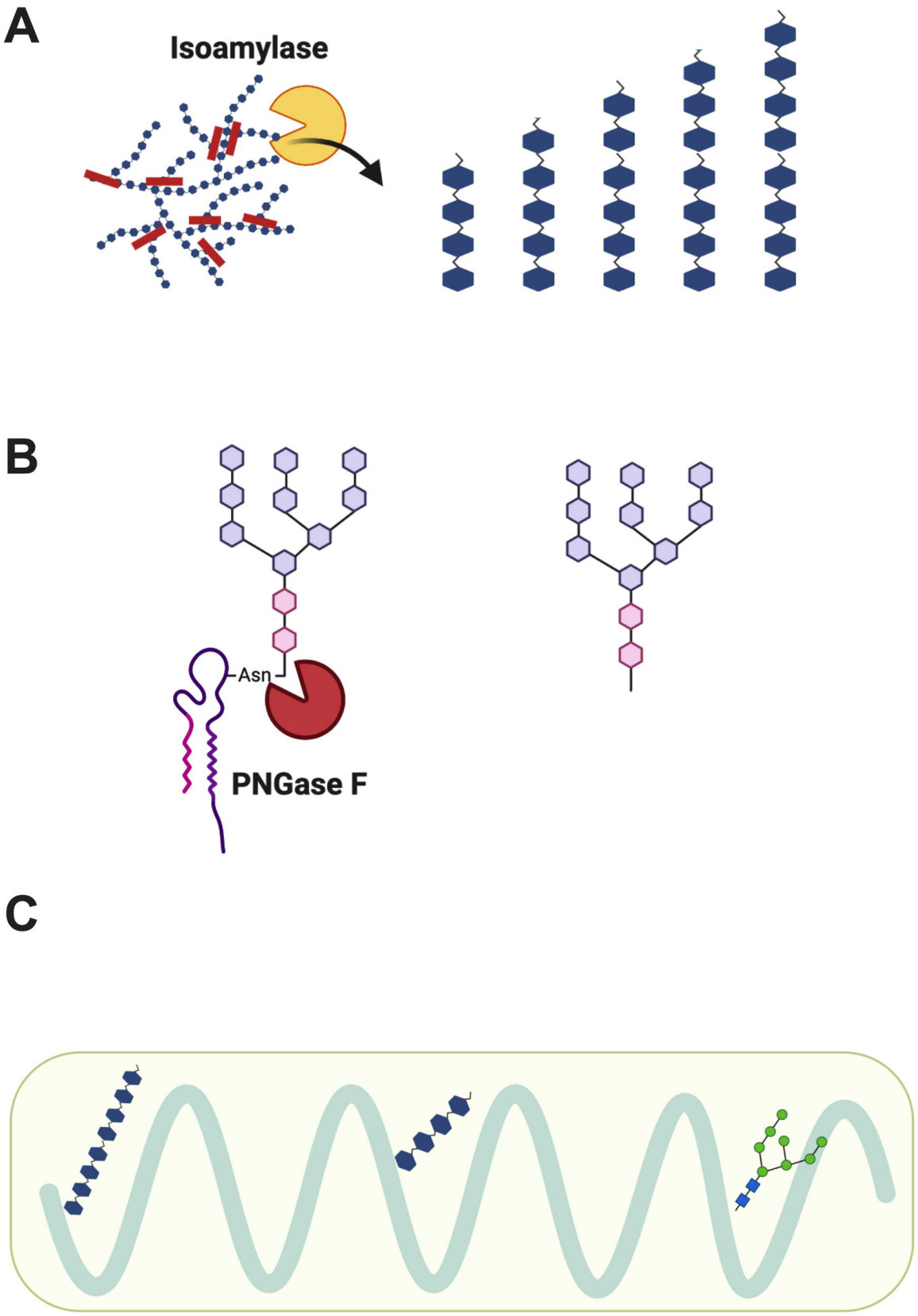
A
Isoamylase
B
Asn
PNGase F
C

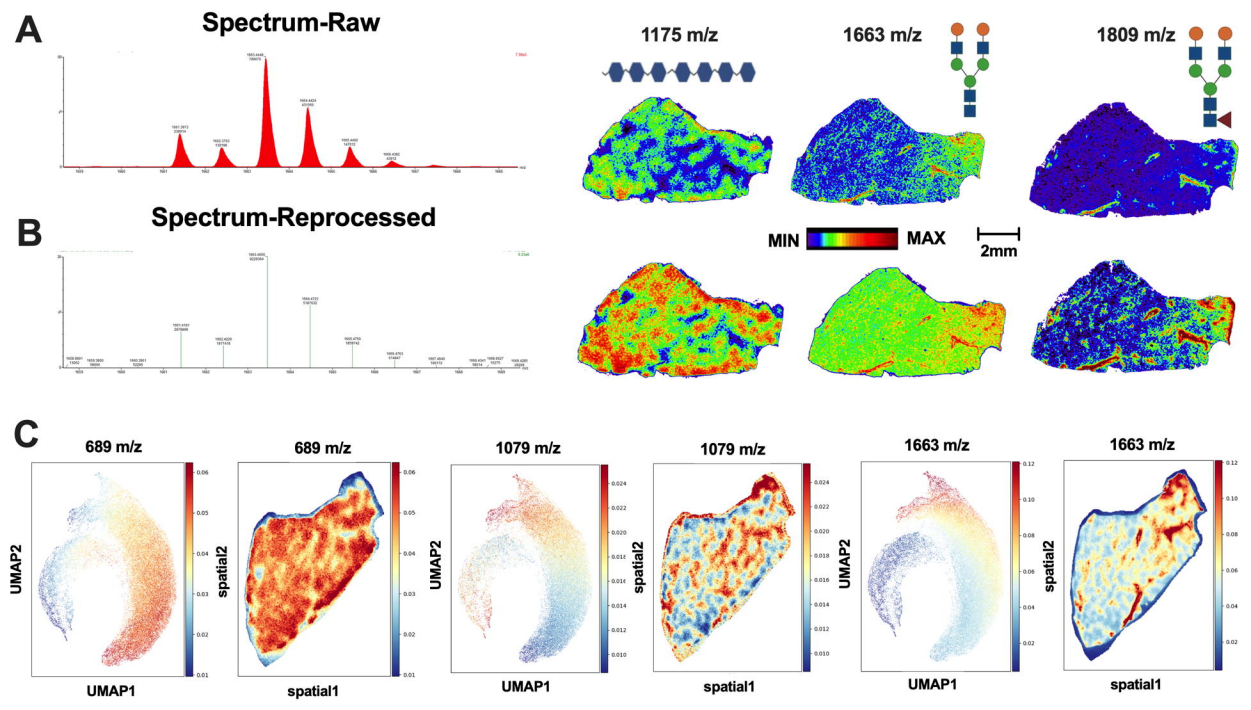
A
Spectrum-Raw
B
Spectrum-Reprocessed
1175 m/z
1663 m/z
1809 m/z
MIN
MAX
2mm
C
689 m/z
689 m/z
1079 m/z
1079 m/z
1663 m/z
1663 m/z
UMAP2
UMAP1
spatial2
spatial1

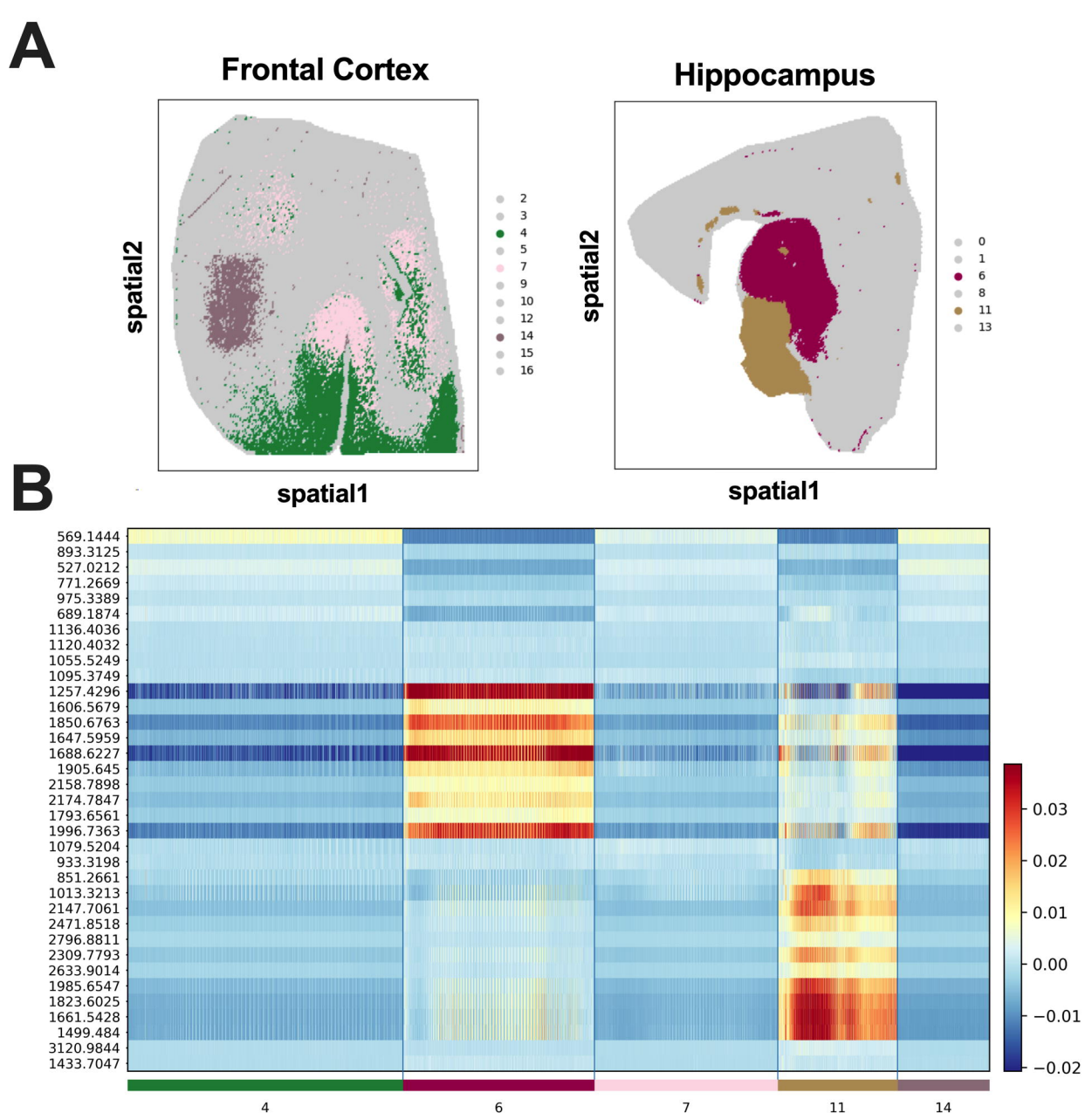
A
Frontal Cortex
spatial2
spatial1
2
3
4
5
7
9
10
12
14
15
16
Hippocampus
spatial2
spatial1
0
1
6
8
11
13
B
569.1444
893.3125
527.0212
771.2669
975.3389
689.1874
1136.4036
1120.4032
1055.5249
1095.3749
1257.4296
1606.5679
1850.6763
1647.5959
1688.6227
1905.645
2158.7898
2174.7847
1793.6561
1996.7363
1079.5204
933.3198
851.2661
1013.3213
2147.7061
2471.8518
2796.8811
2309.7793
2633.9014
1985.6547
1823.6025
1661.5428
1499.484
3120.9844
1433.7047
0.03
0.02
0.01
0.00
−0.01
−0.02
4
6
7
11
14

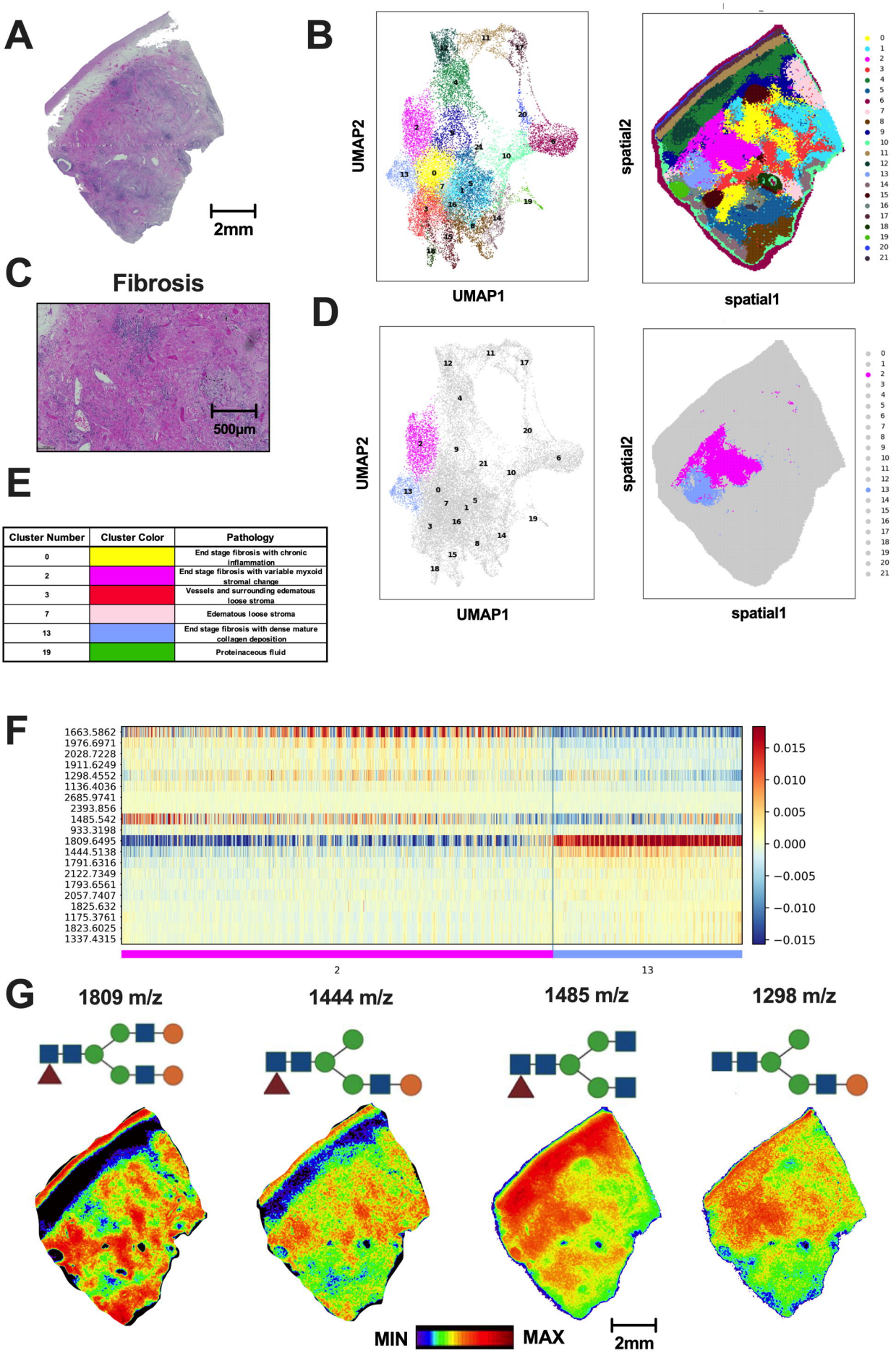

Cluster Number	Cluster Color	Pathology
0		End stage fibrosis with chronic inflammation
2		End stage fibrosis with variable myxoid stromal change
3		Vessels and surrounding edematous loose stroma
7		Edematous loose stroma
13		End stage fibrosis with dense mature collagen deposition
19		Proteinaceous fluid

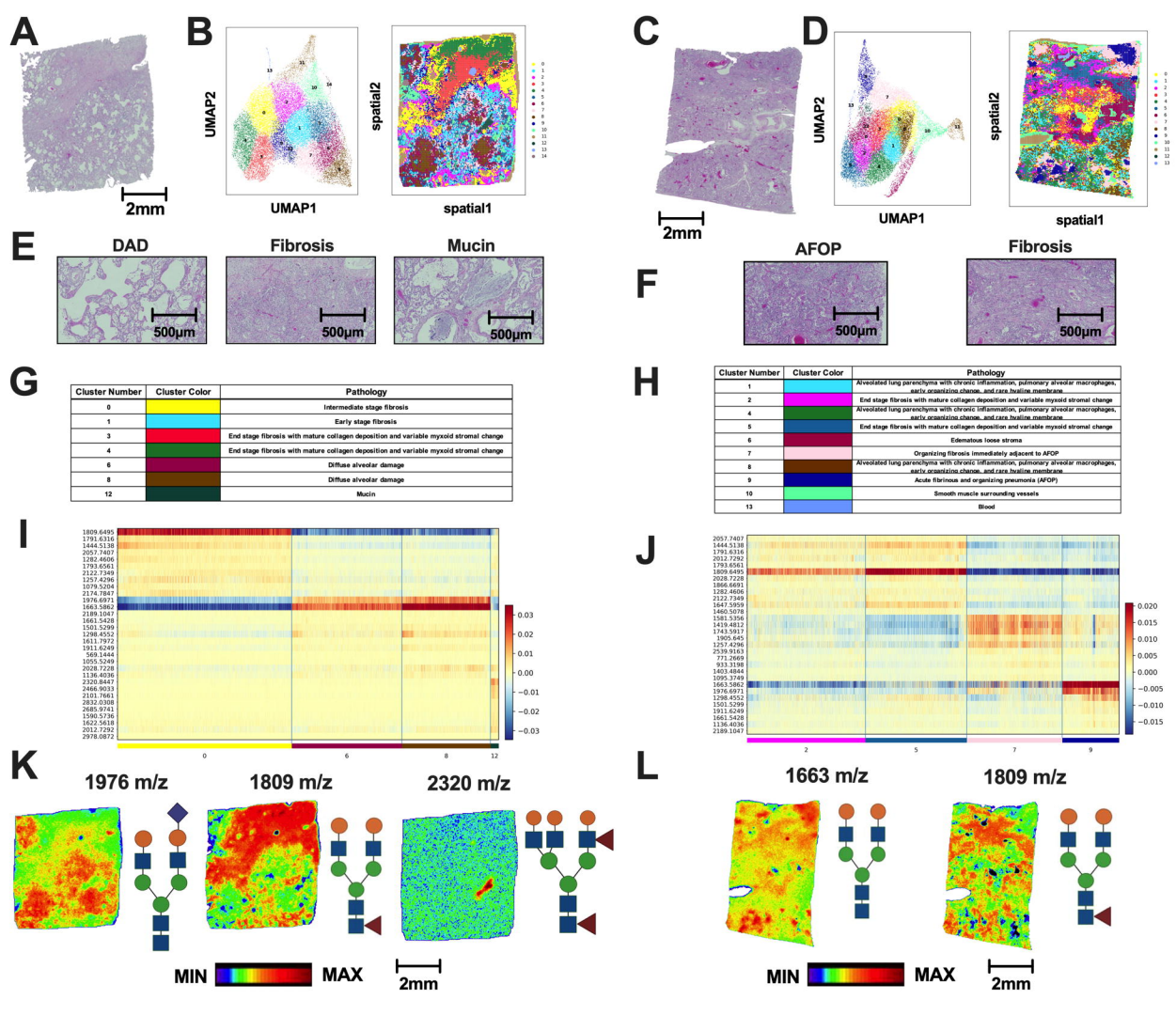

Cluster Number	Cluster Color	Pathology
0		Intermediate stage fibrosis
1		Early stage fibrosis
3		End stage fibrosis with mature collagen deposition and variable myxoid stromal change
4		End stage fibrosis with mature collagen deposition and variable myxoid stromal change
6		Diffuse alveolar damage
8		Diffuse alveolar damage
12		Mucin

Cluster Number	Cluster Color	Pathology
1		Alveolated lung parenchyma with chronic inflammation, pulmonary alveolar macrophages, early organizing change, and rare hyaline membrane
2		End stage fibrosis with mature collagen deposition and variable myxoid stromal change
4		Alveolated lung parenchyma with chronic inflammation, pulmonary alveolar macrophages, early organizing change, and rare hyaline membrane
5		End stage fibrosis with mature collagen deposition and variable myxoid stromal change
6		Edematous loose stroma
7		Organizing fibrosis immediately adjacent to AFOP
8		Alveolated lung parenchyma with chronic inflammation, pulmonary alveolar macrophages, early organizing change, and rare hyaline membrane
9		Acute fibrinous and organizing pneumonia (AFOP)
10		Smooth muscle surrounding vessels
13		Blood

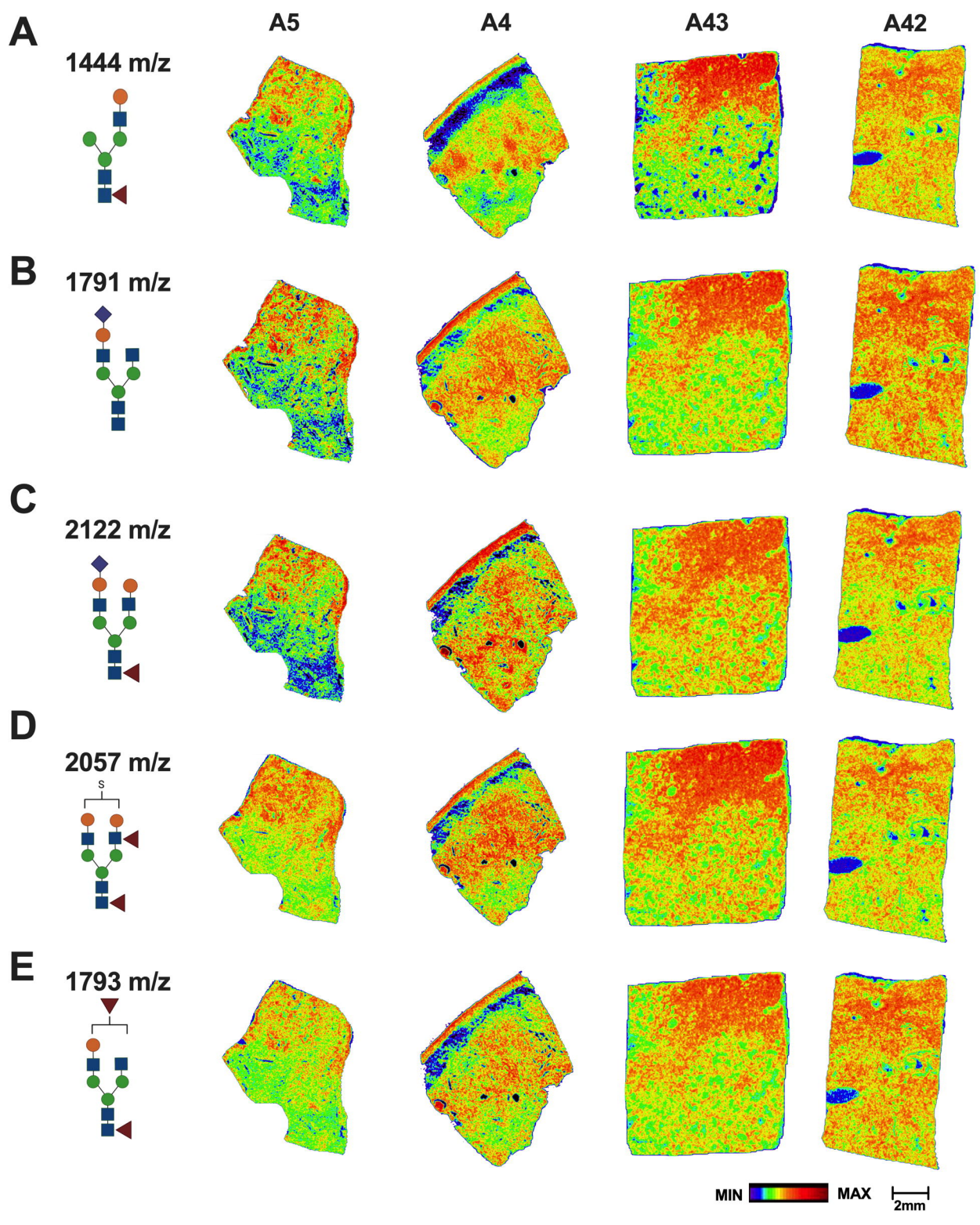
A
A5
A4
A43
A42
1444 m/z
B
1791 m/z
C
2122 m/z
D
2057 m/z
S
E
1793 m/z
MIN
MAX
2mm